Design, Simulation, and Implementation of Two Novel Micromechanical Vibratory-Rate Gyroscopes

by

Michael Kranz

advised by

Dr. Gary Fedder

second reader

Professor William Messner

in partial fulfillment of the requirements for a Masters degree in the

Department of Electrical and Computer Engineering

at

Carnegie Mellon University

May, 1998

Contents

I. Introduction

Microelectromechanical systems (MEMS) technology holds the promise of making complex systems that integrate micromechanical and microelectronic components. These complex systems will be extremely small in size and inexpensive when batch fabricated. A particular class of complex systems that is being explored is that of inertial sensors. Systems such as accelerometers and gyroscopes can be implemented in a small package at a small cost, and provide high performance while being rugged and operable in harsh environments. In particular, a MEMS gyroscope system would be orders of magnitude less expensive and take up less space than the macro-systems available.

A number of individuals and groups have worked on micromechanical vibratory-rate gyroscopes with varying designs, and implemented in different fabrication processes. Bernstein [1] demonstrated a tuning fork gyroscope in which two masses oscillate laterally. An external rotation induces oscillation out of the plane of the device. Boeing is now developing a commercial version of this design. Juneau [2] demonstrated a gyroscope with a rotating mass, where deflections induced by rotations about two axes were also measured out of the plane of the device. Clark [3] described a gyroscope with a single mass oscillating laterally, and with lateral rotation induced deflections sensed capacitively. A gyroscope based on a vibrating ring was demonstrated by Putty [4]. The work presented in this thesis focuses on two new designs that reduce some of the numerous sources of measurement error in gyroscopes.

An initial consideration in MEMS design is the fabrication process that will be used. The main process used in this work is a combination of a CMOS process offered by an outside vendor, and a set of post-processing steps done here at Carnegie Mellon University [5]. This process provides a composite structural material that allows for novel designs, a straightforward integration of electronics with the microstructure, and a scalable process. However, the composite structure leads to problems with curvature resulting from gradients in residual stresses. In addition, the post-CMOS micromachining steps are not mature and are a subject of parallel research.

The two gyroscopes being explored are in the class known as vibratory-rate gyroscopes. This class

of devices must be mechanically excited in resonance to measure the rotational rate of the device. A configuration of mass is forced to oscillate in a specific mode. When the device experiences an external rotation, the velocity of the mass results in a Coriolis force acting on the mass in the frame of reference of the device. This force acts in a direction orthogonal to the velocity of the mass. The resulting oscillatory motion is then sensed in some fashion and a rotational rate signal derived from it.

There are two primary ways of configuring these devices. In one configuration, resonance matching, the excited mode is a resonant mode and a large displacement is developed due to the Q-factor of the structure. The sensed mode is designed to have nearly the same resonant frequency as the excited mode. Then, when the Coriolis force excites that mode, another gain of Q is seen. The second configuration, resonance separation, uses two modes that are separated in resonant frequency. The sensed mode is then a controlled mode that operates similarly to an accelerometer and measures the Coriolis acceleration.

The two designs in this thesis attempt to reduce sources of measurement errors seen in micromechanical gyroscopes [7]. One device, the three-fold symmetric gyro (3FSG) operates using a matched resonant frequency configuration. This device uses a completely symmetric structure to ensure that the two oscillation modes are matched through process variations and environmental conditions. The second device, the elastically-gimbaled gyroscope (EGG) can be designed using either system configuration, but has only been implemented in the matched resonant frequency configuration. This device places one mass, constrained to motion in only one direction, within a second mass that is constrained to move only in the orthogonal direction. Completely separating oscillation modes reduces errors due to mechanical crosstalk.

Simulation of the gyroscope systems, and MEMS in general, is important in the design and verification of these devices. Mechanical simulation can and is done using a finite element package. However, that strategy will not simulate the interactions of the mechanical elements with electrostatic elements, electronics, and controls. The design and modeling of these gyroscopes contributed to the motivation for and the development of a multidomain MEMS simulation methodology, NODAS [9][10][12]. A hierarchical multi-domain nodal simulation methodology is being developed here at CMU, and the two gyroscope

4

devices have been important testbeds for the development, testing, and verification of the simulation tools. The devices have also motivated modeling of components for the tools. Beams with effective mass and plate masses that include global inertial effects due to rotation, were important components in the simulation of these gyroscopes.

Two generations of both gyroscopes have been implemented and fabricated at the point of this writing. The 3FSG has been fabricated in both a polysilicon process and the CMOS-MEMS process, but only the CMOS-MEMS version will be discussed here. The EGG has only been fabricated in CMOS-MEMS, as the structure cannot be operated usefully if fabricated in a polysilicon process. Simulations of the mechanical structures have been performed using finite element analysis in ABAQUS, and multidomain nodal simulations have been performed in Saber [15]. Due to delays in the CMOS-MEMS processing, devices have only now been released and only initial testing has been performed for this report. Future directions for design, simulation, and test are outlined in the conclusions.

II. CMOS-MEMS Processes

The microfabrication process is fundamental to the performance, operation, and design of most MEMS devices. Inertial sensors are especially sensitive to the fabrication process. Minimum lines and widths define the ranges of elasticity and resonant frequency that can be attained. The stability of the material affects performance of the device with variations in temperature and other conditions, and over time. The ease with which electronics are integrated, the performance of the electronics, and the performance of that integration can greatly affect the entire device performance.

At Carnegie Mellon, mechanical structures have been integrated with CMOS using the Hewlett-Packard 0.5µm three-metal n-well CMOS process available through the MOS Implementation Service (MOSIS). To produce a suspended microelectromechanical structure, the metal and dielectric layers combine to form composite structural elements [5]. The process flow in Figure 2 shows the development of a high-aspect-ratio beam in cross-section.

The dice have CMOS circuits covered by the metal-3 and oxide layers as shown in Figure 2a. The
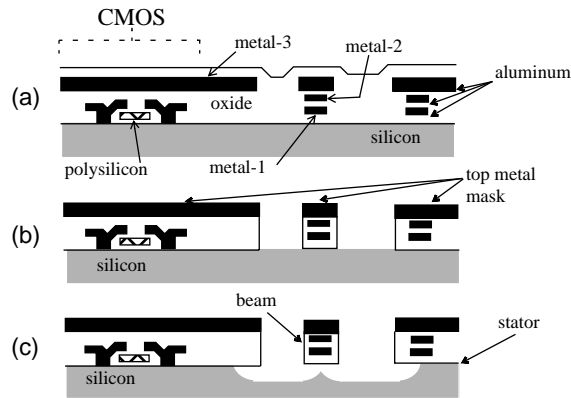
Fig.2 - Cross-sections of the process flow. (a) After CMOS processing. (b) After anisotropic oxide etch. (c) After isotropic silicon etch.

top metal layer is used as an etch-resistant mask during the subsequent dry etching that creates the composite microstructures. The microstructural sidewalls are formed by directionally etching the top oxide layers down to the substrate. Areas not covered by metal are anisotropically etched in a two step CHF_3/O_2 reactive ion etch (RIE), resulting in the cross-section shown in Figure2b. In Figure 2c, a final SF_6/O_2 low-power isotropic silicon etch releases the structure from the substrate. The dry-etch release prevents breakage and sticking of structures to the substrate and to each other.

This process allows production of beams with a minimum width of 1.5μm and a maximum width of up to 25μm. Beams can be comprised of any combination of metal-1, metal-2, or metal-3, and with or without an additional polysilicon layer. A full metal-1, metal-2, and metal-3 beam, composing most of the structures, has a thickness of approximately 5μm, Young's modulus of 62GPa, and minimum width of 1.5μm[8]. Minimum gap widths and maximum beam widths depend on the amount of masked and empty area surrounding them.

An important feature of this process is the ability to fabricate electronic devices adjacent to the mechanical structures to produce a completely integrated microelectromechanical device. The CMOS devices must be inset by at least 30μm from the side of an etched pit in order to survive the etching processes that releases the mechanical structures. The short path between structures and circuits results in small parasitic capacitances to the substrate. It is possible to have less than 10fF of parasitic capacitance on

the mechanical structures.

A second key feature of the process is the production of composite structures made up of multiple conductors separated by dielectric layers. This allows numerous wiring schemes within a single mechanical structure. The mechanical structures are defined by only the topmost metal layer, which remains after the etching process. The other two metal layers and the gate polysilicon layer are available as additions to the structure, for either mechanical interconnect or electrical interconnect. A suspended mechanical structure need not be constrained at a single electric potential. Various parts of the suspended structure, through the use of the metal layers as interconnect, can be placed at different potentials.

This process has a couple of disadvantages that must either be accepted or accommodated by design, preferably the latter. One problem is the limited undercut of mechanical structures by the last silicon etch. The lateral etch rate of Si is reduced in small holes. Large plate masses need to be composed of relatively large holes, 6μm x 6μm, between relatively small structural elements, again 6μm. The largest releasable structure ranges in width from 6μm to 25μm depending on the amount of empty space near the structure. This drastically reduces the amount of available mass per a given plate size. Mass is a key component in inertial sensors, so this represents a serious drawback.

The second problem to overcome is that of structure curvature. The composite microstructures are composed of materials that have different residual stresses. This yields a non-symmetrical stress gradient in the microstructure. Upon being released, the structures tend to curl up out of the plane of the device. The radius of curvature depends on the actual composition of the structures, and can range from 1mm to 10mm. On average, the radius of curvature is about 2mm. This curvature can be disastrous for larger structures where comb drives become misaligned and masses no longer move in plane.

Inertial sensors see sensitivity increases with increases in mass. Currently in the CMOS-MEMS process, increasing the mass means increasing the area of the device. However, the curl of the structures becomes a major issue in the design. Curling frames (to be discussed in section IV-A) were implemented to relieve some of the curling problems, but lead to other problems. Device wiring needs to be routed a long
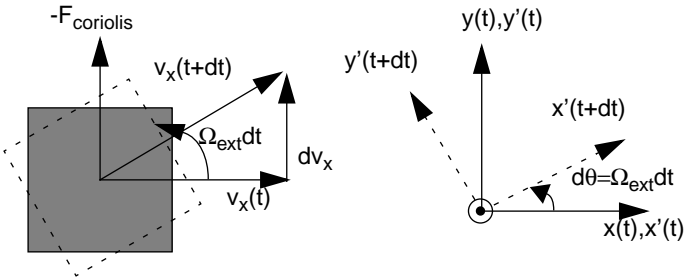
Fig. 3 - For a mass moving with velocity V_x in the global frame of reference (x, y), a local rotating frame of reference (x, y) sees a rotation of the velocity vector, the Coriolis acceleration.
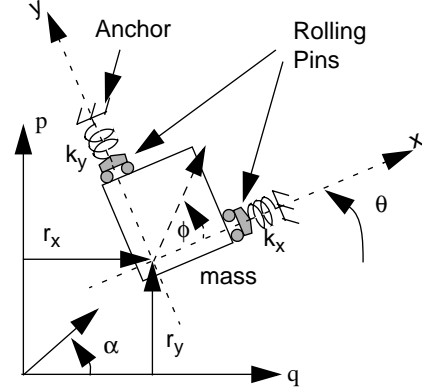
Fig. 4 - Schematic representation of a simple mass spring system with two orthogonal modes.

distance from the mechanical structure to the circuits through the frame. Even though parasitic capacitances to the substrate are small, but interlayer capacitances can be large. When wiring through the frame, the segments of the frame that carry signal lines need to have either all three metal layers dedicated to the signal, or the middle metal layer can be used to carry the signal while the top and bottom layers are driven by a buffer and shield the inner signal line.

III. General Vibratory-Rate Gyroscope Principle

In general, vibratory-rate gyroscopes use a proof mass suspended by a elastic suspension and oscillating in a specific fashion. Figure 3 shows a mass is moving with velocity v_x in a stationary frame of reference (x, y). Both the mass and a local frame of reference, (x', y'), are experiencing an external rotation, θ, around the z-axis at a rotational rate, Ω. There are no external forces acting on the mass, so the mass' velocity vector must remain constant in the global frame. Therefore, the velocity vector appears to rotate in the local frame. That acceleration in the local frame is called the Coriolis acceleration, a_c. From this acceleration, a pseudo-force is derived, the Coriolis force. This force, F_c, acts orthogonal to the velocity in the local frame and is proportional to the external rotation rate.

$$F_c = m\frac{d}{dt}(v_x) = -2mv_x\Omega \tag{1}$$

A typical vibratory-rate gyroscope consists of a mass-spring system that has at least two orthogonal modes of oscillation (Figure 4). The mass is forced to have an oscillatory velocity in the frame of reference

8

of the device. When the device experiences a rotation, the Coriolis force induces oscillation of the orthogo-

nal mode of the device. Sensors detect this motion and provide a signal from which the rotational rate is

extracted.

The equations of motion for a mass-spring system moving in a noninertial reference frame are found

using Lagrangian dynamics [11]. First, expressions for the potential energy and kinetic energy of the sys-

tem must be found. The variables used in the expressions are shown in Figure 4. The global frame of refer-

ence is the p-q-α frame, the local frame of reference, x-y-ϕ, is rotated by an angle, θ, with respect to the

global frame. The local frame is also translated by r_x and r_y with respect to the global frame.

The potential energy is stored in the springs:

$$PE = \frac{1}{2}k_x x^2 + \frac{1}{2}k_y y^2 + \frac{1}{2}k_\phi \phi^2 \tag{2}$$

The kinetic energy is calculated in the global frame of reference, using the global variables:

$$KE = \frac{1}{2}m\left(\frac{dq}{dt}\right)^2 + \frac{1}{2}m\left(\frac{dp}{dt}\right)^2 + \frac{1}{2}I\left(\frac{d\alpha}{dt}\right)^2 \tag{3}$$

The global variables are related to variables in the local frame of reference by a rotation matrices:

$$q(t) = \cos(\theta)x(t) - \sin(\theta)y(t) + r_x(t) \tag{4}$$

$$p(t) = \sin(\theta)x(t) + \cos(\theta)y(t) + r_y(t) \tag{5}$$

$$\alpha(t) = \theta(t) + \phi(t) \tag{6}$$

The equations of motion (EOM's), in the local frame of reference, are found from [11]

$$F_{x_i} = \frac{\partial L}{\partial x_i} - \frac{d}{dt}\frac{\partial L}{\partial x_i} \tag{7}$$

where x_i are the generalized coordinates, F_{xi} are external forces such as the damping and excitation forces,

and L is the Lagrangian ($L=KE-PE$).

The global coordinates in the kinetic energy relation are substituted by (4), (5), and (6) to convert to

local coordinates. Equation (7) is then applied for each of the on-chip coordinates, (x, y, ϕ), by replacing

the generalized coordinate by the respective on-chip coordinate, yielding:

$$\ddot{x} = -\omega_x^2 x - \frac{\omega_x}{Q}\dot{x} - \frac{F_x}{m} + x\Omega^2 + y\dot{\Omega} + 2\Omega\dot{y} - a_x\cos\theta - a_y\sin\theta \tag{8}$$
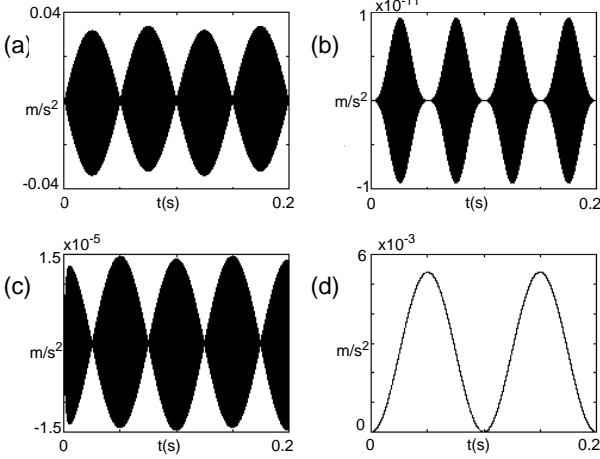
Fig.5 - Individual EOM terms. (a) Coriolis acceleration. (b) Centripetal acceleration. (c) Angular acceleration. (d) Linear acceleration in the local frame of reference
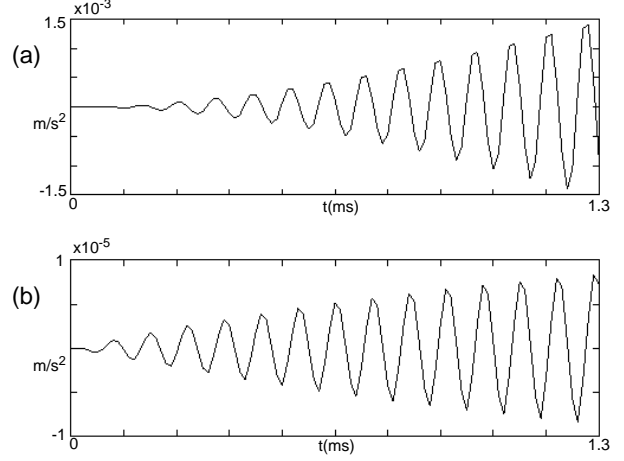
Fig.6 - Close up of the Coriolis acceleration (a), and the angular acceleration term (b). Upon closer examination, a 90 degree phase difference is seen.

$$\ddot{y} = -\omega_y^2 y - \frac{\omega_y}{Q}\dot{y} - 2\Omega\dot{x} + y\Omega^2 - x\dot{\Omega} + a_x\sin\theta - a_y\cos\theta \tag{9}$$

$$I\ddot{\phi} = -k_\phi\phi - I\ddot{\theta} \tag{10}$$

where $\omega_x^2 = k_x/m$, and $\omega_y^2 = k_y/m$, are the resonant frequencies of the x and y modes, respectively, a_x and a_y

are external accelerations, and Q is the quality factor of resonance. The Coriolis accelerations are the $2\Omega\dot{y}$

and $2\Omega\dot{x}$ terms. The last two terms in (8) and (9) are acceleration terms which create transients at the nat-

ural frequency of the system. The terms $y\dot{\Omega}$ and $x\dot{\Omega}$ refer to the inertia of angular acceleration. The $y\Omega^2$

and $x\Omega^2$ are centripetal accelerations, and act as spring softeners.

For this and future discussion, motion in x will be the excited mode, and motion in y will be the

sensed mode. If a sinusoidal force source with frequency ω_x is used to drive the excited mode,

$$F_x = F_d\sin(\omega_x t) \tag{11}$$

the displacements in x and y will also be sinusoidal with that same frequency.

A simulation in Matlab was performed to determine relative sizes and phases of these unwanted

terms compared to the important Coriolis terms for a typical micromechanical vibratory-rate gyroscope

experiencing a 10°/sec rotational rate. Figure 5a is a plot of the Coriolis acceleration, which is at the natural

frequency and has an amplitude of 0.03 m/s². Figure 5b is a plot of the centripetal acceleration. This term

has a much smaller amplitude of $0.9x10^{-11}$m/s^2, and will get larger with higher rotational rates. Figure 5c

plots the acceleration due to the external angular acceleration. This term has an amplitude of $1.5x10^{-5}$m/s^2,

which is 2000 times smaller than the Coriolis force. In this situation, the angular acceleration is closest in

magnitude to the Coriolis force, and will get larger with higher angular accelerations of the device. Figure

6 compares this term and the Coriolis term more closely. From this plot, it can be seen that these terms are

90 degrees out of phase. Figure 5d plots the acceleration in the local frame of reference due to external

accelerations that the device is experiencing. This signal is not at the natural frequency of the device, as the

other signals are.

Many of these unwanted terms can be cancelled through proper system design. Controlling the

excited mode so that it oscillates at its natural frequency with a constant amplitude cancels many of the

terms that affect the excited mode. The spring softening effect can be compensated through tuning the

mode frequencies electrostatically. External linear accelerations are removed through demodulation and

filtering, and through using two or more devices that operate differentially.

A myriad of other error terms can occur in gyroscopes. These errors are caused by processing varia-

tions, design issues, temperature fluctuations, design requirements, etc. In a gyroscopic system, there will

be a zero-input bias signal and a scale factor. One of the most serious problems is the drift of these values

over time and temperature. This drift is indistinguishable from a rotation signal.

A vibratory-rate gyroscope can be designed to be put into the system shown in Figure 7. The pur-

poses of the system are to reliably and accurately excite the system, and to sense and process the output

signal. The system is also used to cancel or reduce some of the unwanted signals. The majority of this work

has been focused on the mechanical structure. The rest of the system has been determined, but actual

design of system parameters and fabrication of the on-chip and off-chip electronics has not been per-

formed.

Comb-drive capacitive position sensors are used to sense displacement of the sensed mode (these
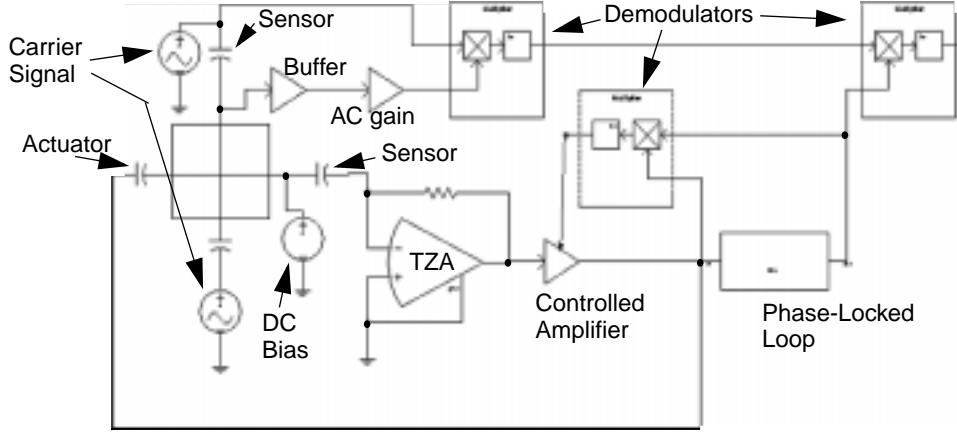
Fig.7 - Basic system block diagram for a vibratory-rate gyroscope.

will be shown in section IV-A), and are set up as a voltage divider across which a high-frequency carrier

signal is placed. Using a parallel-plate approximation, the capacitance for a comb drive is given by

$$C = \frac{2N\varepsilon_o h(l_o - y)}{g_o} \tag{12}$$

where N is the number of comb fingers, h is the height of the fingers, g_o is the gap between fingers, l_o is the

initial overlap of comb fingers, and y is the displacement from that initial overlap.

For a capacitive voltage divider, the voltage at the center of the divider is at the frequency of the car-

rier signal, and has an amplitude of

$$V = \frac{C_2 V_m}{C_1 + C_2} = \frac{V_m}{2} + \frac{y V_m}{2l_o} \tag{13}$$

With l_o=20μm in the second-generation designs, and a carrier signal amplitude of 10V, the voltage output

has an amplitude of 0.25 V/μm.

The rest of the system is implemented as follows. The excited mode is set up in a positive feedback

loop using a feedback amplifier with a controlled gain. One comb drive on the excited mode is used as an

actuator, and one is used as a sensor. The sensor has a DC bias on one side, and a transimpedance amplifier

(TZA) on the other side. When the excited mode oscillates, a displacement current is sensed by the tran-

simpedance amplifier. The amplitude of this current is

$$i = V\frac{dC}{dt} = \frac{V2N\varepsilon_o h}{g_o}\frac{dx}{dt} = \frac{V2N\varepsilon_o h}{g_o}x_o \omega_x \sin(\omega_x t) \tag{14}$$

A second amplifier with a controlled gain is used to further amplify the voltage. This signal is sent back to the actuators in a positive feedback loop. Brownian motion will create a signal for the amplifier without the structure being excited. This signal will be amplified and sent back to excite the structure. The oscillation will build up until the setpoint of the controlled amplifier is reached. As a result, over various environmental conditions, the structure will oscillate at its natural frequency and with a constant amplitude. The output of the controlled amplifier is also sent to a phased-lock loop to provide a constant amplitude reference signal at the natural frequency of the structure for use in sensor output demodulation.

When experiencing a rotation, the sensed mode of the device will be excited, and a voltage will be seen by the buffer at the center of the capacitive voltage divider. This signal will be at the frequency of the carrier signal, and be modulated by the position signal of the sensed mode. This position signal is, itself, a signal with a carrier at the natural frequency of the device, modulated by the external rotation rate.

$$V_o \propto \Omega \sin(\omega_c t) \sin(\omega_r t) \tag{15}$$

Determining the rotational rate requires two demodulation steps. The first demodulator demodulates the output signal with the clock used to provide the capacitive-position-sense carrier signal. The second demodulator separates the rotational-rate signal from the natural frequency of the resonance. After filtering, the final signal will represent the rotational rate the system is experiencing.

IV. Three-Fold Symmetric Gyroscope Design

A. Implementation

Two generations of the three-fold symmetric gyroscope (3FSG) are shown in Figures 8 and 9. In both designs, a central proof mass is surrounded by a three-fold symmetric suspension consisting of identical spring sets along both the x and y modes. In the first generation, a set of simple beams and folded flexures are placed symmetrically about the device. In the second generation, only simple beams are used. The suspension connects the plate masses to the comb-finger actuators and sensors, and connects everything to the substrate anchors.

The comb-finger actuators apply an electrostatic force to the proof mass in the x-direction, exciting

Flexures

Plate Mass

Comb-Finger Actuator

Comb-Finger Sensor

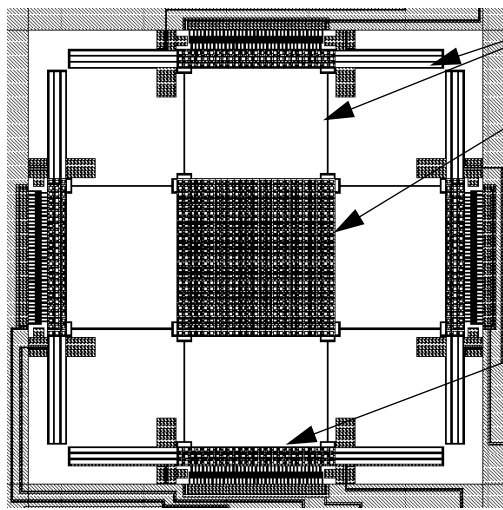Doubly-Gimbaled Frame

Substrate Anchor

Fig.8 - Three-fold symmetric gyroscope design with the electrostatic drive along the x-axis, and a capacitive displacement sensor along the y-axis.
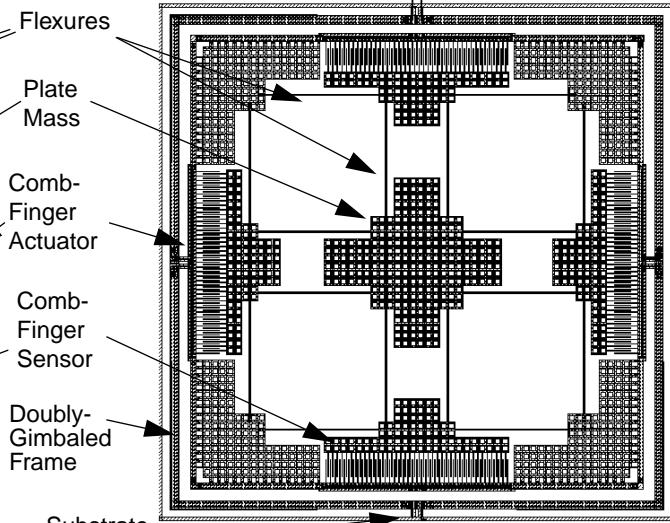
Fig.9 - Second-generation of the Three-Fold SYmmetric Gyroscope fabricated in CMOS.

the driven mode. When experiencing a constant external rotation, the Coriolis force acts along *y* and has a frequency equal to that of the excitation frequency. The *Q*-factor of the system provides a gain in the displacement of the sensed mode. The *y* deflection is sensed with a pair of comb-finger capacitors connected as a differential capacitive voltage divider. A unity-gain buffer detects the divider's voltage and drives off-chip circuitry.

The suspension is three-fold symmetric in that there is symmetry along *y*, along *x*, and along the diagonal. The suspension serves two purposes. First, the driven and sensed modes of the device displace different, but identical, spring sets; one set displaces in *x* and one set displaces in *y* (See Figure 10, a finite-element simulation of the oscillation modes of the first design). Spring constants as well as moving mass are matched along both modes. Therefore, both oscillation modes have equal resonant frequencies. The modes will theoretically match even through a uniform process variation, *e.g.*, overetching of the proof mass, and through time and temperature variations.

The second purpose of the suspension is to decouple, mechanically, the *x* and *y* deflections of the actuators and sensors. The suspension allows motion of the central mass in both *x* and *y* by using complete springs that are very stiff in one direction and very compliant in the other, as an approximation to a rolling

pin. The masses that attach to the actuators and sensors are placed in the suspension in such a way that they can only move along one axis. So, a deflection of the proof mass in *x* will not affect the sense mass, which only moves in *y*. The spring network reduces the mechanical crosstalk between the sensors and actuators. There is second-order crosstalk, however. When the proof mass displaces in *x*, the sense masses pull in towards the proof mass because of the constant length of the connecting beams (see Figure 10).

The second-generation device also includes a doubly-gimbaled frame around the entire device. The frame has two purposes. The main purpose is to reduce susceptibility to problems associated with structure curvature. The average out-of-plane radius of curvature for the CMOS 0.5µm process is 2mm. The 3FSG is approximately 600µm long. The out-of-plane height of the edge of the device with respect to the center of the device is given by

$$h = r - \sqrt{(r^2 - l^2)} \qquad (16)$$

In this scenario, the out-of-plane height will be 23µm. With the device anchored at the outside edges, the center of the device must be sunk below the height of the substrate by 23µm. That approaches the depth of the silicon etch that releases the device, and the device could actually scrape along the substrate and be inoperable. Even if the etch were deep enough, the curvature also results in the released comb drives curling up at a 8.6º angle with respect to the comb drives that are anchored to the substrate. This reduces the capacitance of the comb drive, making the sensors less sensitive, and yielding less force from the actuators. The double frame allows all of the components of the actual device to curl freely, although the frame may experience misalignment with itself.

The second purpose of the frame is to relieve residual stress. The first-generation design used folded flexures to ensure that upon release, the flexures would not buckle. If simple beams were used in the first design, they would form a fixed-fixed structure that is very susceptible to buckling. In the second design, however, the doubly-gimbaled frame can expand in both *x* and *y* to relieve stress. The device expands with the frame. Therefore, simple beams can be used. The use of simple beams is preferred because beams are very stiff in one direction, and the actuator and sensor masses are decoupled more efficiently.
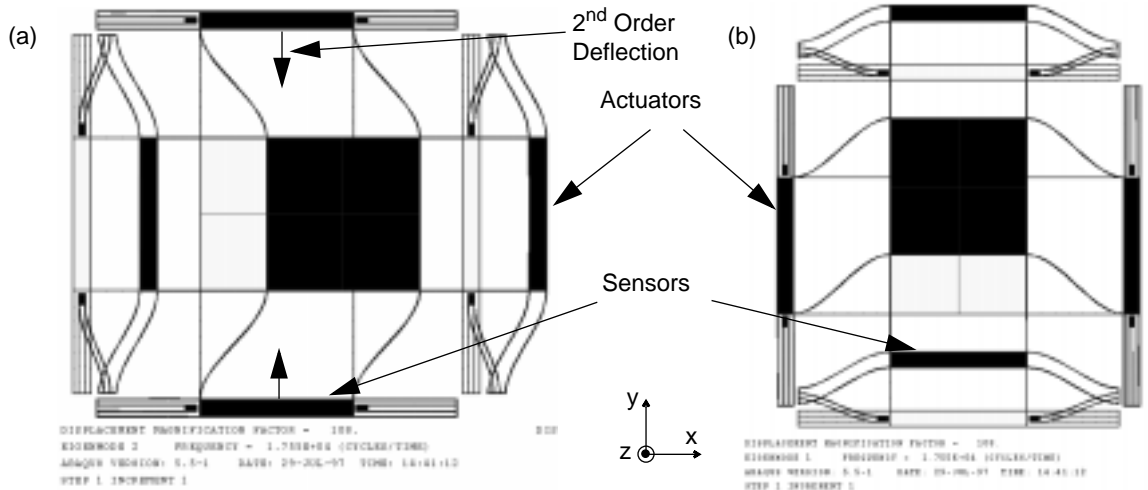
Fig.10 - FEM simulations showing deflection of the mechanical structure in both modes. The grey outline is the undisplaced device, the black outline is the displaced device.(a) Driven *x*-mode.(b) Sensed *y*-mode.
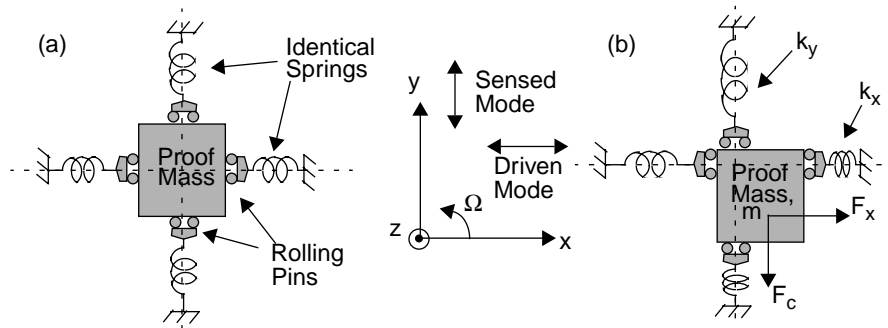

Fig.11 - Schematic diagrams of the three-fold symmetric gyroscope, (a) stationary, (b) deflected under forces in *x* and *y*.

B. Structure fundamentals

The three-fold symmetric vibratory-rate gyroscope is shown in schematic in Figure 11a. The implementation attempts to most ideally replicate this schematic consistent with the capabilities of a surface micromachining process. The suspension approximates a set of identical springs placed symmetrically about the central mass and providing a rolling pin condition for the mass' motion. Deflection of the mass in *x* and *y* is depicted in Figure 11b. The rolling pins constrain the springs to act only along the *x* or *y* axis. Therefore the restoring forces on the mass are always orthogonal and in line with the *x* and *y* axes. The two fundamental modes of oscillation are along the *x*-axis, the driven mode, and the *y*-axis, the sensed mode. The equations of motion (EOM's) for this gyroscope are found using a Lagrangian analysis, and are identi-

cal to those described in section III (equations (8), (9), and (10)).

If the forcing function, F_x, is at the resonant frequency of the driven mode, then the displacement of

the proof mass is maximized, with a gain of Q over the static displacement. The frequency of the Coriolis

force is equal to the resonant frequency of the driven mode, with an amplitude modulated by both the max-

imum displacement of the mass in x and the rate of external rotation.

$$F_c = -2m\Omega\dot{x} = \frac{-2m\Omega\omega_x QF_d}{k_x}\sin(\omega_x t) \tag{17}$$

The velocity of the excited mode, the size of the mass, and the external rotation rate determine the

magnitude of the Coriolis force. If the resonant frequency of the sensed mode is equal to that of the driven

mode, $\omega_x = \omega_y = \omega_r$, then maximum displacement for a given rotational rate will occur in the sensed mode.

$$y = \frac{QF_c}{k_y} = \frac{2m\Omega Q^2 \omega_r F_d}{k_x k_y}\cos(\omega_r t) \tag{18}$$

The three-fold symmetric gyroscope implementation inherently matches the resonant frequencies in

both oscillation modes by using a completely symmetric suspension, thereby increasing the sensitivity of

the device by using the Q-factor to maximize displacements for a given force. The symmetry also reduces

effects of process variations on the device sensitivity. In practical implementations of the vibratory-rate

gyroscope, the designed Q value is constrained by the necessary bandwidth of the input rotation. The scale

factor of the device is highly dependent on the matching of the resonant frequencies, since Q is an impor-

tant gain. If the frequencies are not matched, only a fraction of Q will be seen as gain. Through time and

temperature variations, changes in the modes of this device should match, preventing the scale factor from

drifting. Manufacturing variations and offsets may cause some mismatch of the modes, however, so elec-

trostatic tuning may be implemented to compensate.

C. Design

The actual determination of physical parameters for the 3FSG is simple. The highly symmetric struc-

ture reduces the number of variables and equations used in determining the structure parameters. For these

devices, the designs were conservative for the purposes of being able to test the operation. For the most

part that means that the motion of the device could be seen in an optical microscope in the event that on-chip electronics do not work.

Looking specifically at the second generation of the device, the suspension is made up of simple beam springs [13]. In both the x and y directions, there is a total of 8 springs per direction, resulting in a total spring constant for each mode

$$k_x = \frac{8Ehw_x^3}{l_x^3} \qquad k_y = \frac{8Ehw_y^3}{l_y^3} \tag{19}$$

where h is the thickness of the beam, w_x and w_y are widths of the beams along x and the beams along y, respectively, and l_x and l_y are the lengths of the beams along x and beams along y, respectively.

A comb-drive actuator can produce a force, F_d, and a displacement in the excited mode, x_e, of [6]

$$F_d = \frac{1.14N\varepsilon_o h V^2}{g_o} \tag{20}$$

$$|x_e| = \frac{QF_d}{k_x} \tag{21}$$

where g_o is the gap between fingers of the comb-drive, N is the number of fingers, h is the thickness of the fingers, and V is the voltage across the actuator. The factor of 1.14 accounts for nonideality of the actuator due to fringing fields.

The beam springs on the 3FSG are 175μm in length, 2.1μm in width, and 5μm in height. For the CMOS-MEMS process, Young's Modulus, E, is 62GPa. The suspension then has a calculated spring constant of 4.2 N/m in both the x and the y directions. The actuators have 40 comb fingers, separated by a gap of 1.5μm, and a height of 5μm. When driven by 10 V, the actuators produce a force of 0.134μN. The resulting maximum displacement of the excited mode, with a Q of 50, is then 1.6μm. Using (14), the displacement current through the excited mode sensor will have an amplitude of 2.52×10^{-9} A, resulting in a voltage of 2.52mV seen at the output of a transimpedance amplifier with a gain of 1×10^6.

The resonant frequency of the sensed mode (and hence the driven mode) is

$$\omega_{ry} = \sqrt{\frac{k_y}{m}} = \omega_{rx} \qquad (22)$$

Equation (18) developed in section IV-B predicts the magnitude of the sensed displacement, y, given the mass, m, the modes resonant frequency, ω_{ry}, the external rotation rate, Ω, the Q-factor of resonance, and the spring constants. The mechanical sensitivity is then

$$\left|\frac{y}{\Omega}\right| = \frac{2mQ^2\omega_r F_d}{k_x k_y} \qquad (23)$$

The mass on the 3FSG is a 250μm by 250μm plate rearranged in such a way as to put mass on the actuators and sensors, and to reduce the overall area taken up by the device. The actuators and sensors are 20μm wide and 250μm long. The effective density of the composite microstructure is taken to be approximately 2600kg/m^3. The proof mass then has a mass of 0.9425μg, yielding a resonant frequency of 66.76krad/s, or 10.6kHz. When an external rotational rate of 1°/sec is applied, the resulting Coriolis force (17) is 3.42pN. The resulting displacement of the sensed mode is then 40.7pm. Using (13), the final sensitivity for the 3FSG is 10.2μV/°/sec.

Brownian noise will place a limit on the resolution of the device. This noise can be estimated with the following equation [14]

$$\overline{F}_n^2 = \frac{4kT\omega_r \Delta f}{Q} \qquad (24)$$

which will represent a noise in the rotational rate signal of [3]

$$\Omega_n = \sqrt{\frac{kT\Delta f}{mQ\omega_r x^2}} \qquad (25)$$

for a bandwidth of 100 Hz, and at a temperature of 300K, this noise is 0.29°/sec, and is the dominant noise source. This Brownian noise calculation may be misleading, however. Brownian noise is an effect of the conditions of the dissipative forces in the device. The low Q estimate used for this design is partly due to a concern over the internal friction of the composite CMOS-MEMS structure. Data needs to be collected on this internal friction and the Q-factor in vacuum before a more accurate prediction of Brownian noise can be made.
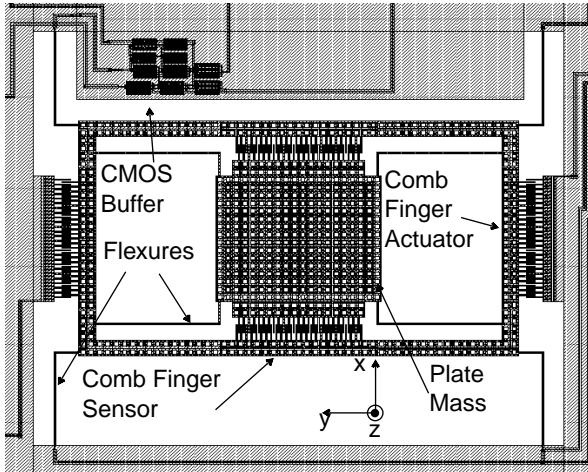
Fig.12 - The elastically gimbaled gyroscope design with the electrostatic drive along the x-axis and capacitive sense of the y displacement.
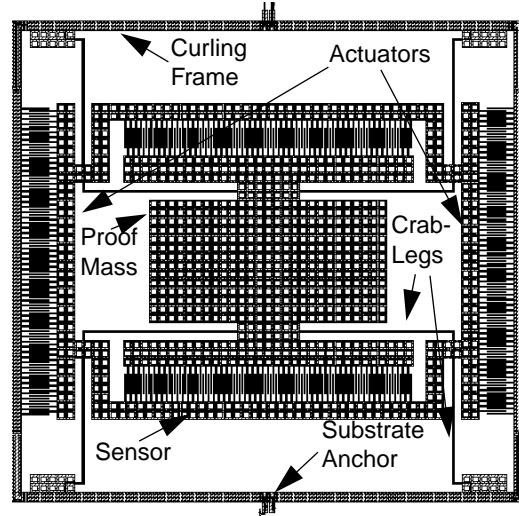

Fig.13 - Second-generation of the elastically gimbaled gyroscope fabricated in the CMOS process.

V. Elastically Gimbaled Gyroscope Design

A. Implementation

Two generations of the elastically-gimbaled gyroscope (EGG) are shown in layout in Figures 12 and 13. This device has an inner mass suspended by a flexure to an outer frame. Similarly, the outer frame is attached to the anchors by a separate flexure. In the second-generation design, these anchors are on a second frame, the curling frame, which performs curl matching. Oscillation of the outer frame is induced by a set of electrostatic comb-finger actuators. An external rotation forces the inner mass to move orthogonally with respect to the outer frame. The motion of the inner mass with respect to the outer frame is sensed by a pair of comb-finger capacitive position sensors that move with the outer frame.

The comb-finger structures that sense and induce oscillation must be independently controlled, even though they are on the same suspended mass. The multiconductor features of the CMOS-MEMS fabrication process allow implementation of this gyroscope. The fabrication process does not require that all suspended structures be homogeneously conducting. Electrical connections to the suspended comb-drive actuators and sensors are made by routing metal interconnect through the suspensions that mechanically connect the inner mass, outer cage, and anchored frame.
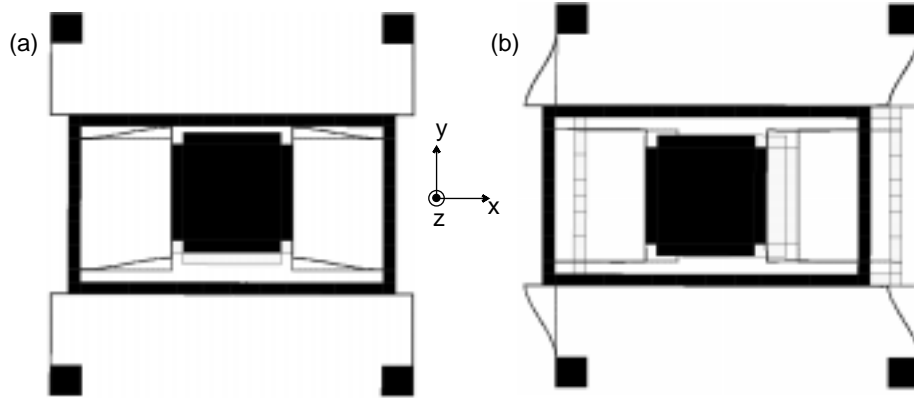
20

Fig.14 - Finite element simulations showing deflection of mechanical structure under x and y forces. (a) Sensed y-mode. (b) Driven x-mode.

Figure 14 shows a finite-element simulation of the motion of this mechanical structure. Note that the decoupling is degraded by the need to have a non-zero x and y compliance in the suspension to relieve residual stress in the composite-beam microstructural material. Therefore, the suspensions on the inner and outer masses cannot be infinitely stiff in one direction, as is desired. Also, because one mass-spring system is nested within the other, the matching of resonant frequencies to obtain a gain in sensitivity due to the Q factor is difficult.

B. Structure Fundamentals

The elastically gimbaled gyroscope is shown in schematic in Figure 15. The design focuses on decoupling the sensed mode from the driven mode by nesting the proof mass and springs within an outer frame, and constraining the motion of the proof mass to the x-axis. The outer frame is then suspended by springs constrained to move only along the y-axis. Mechanical crosstalk is completely eliminated by this design. This reduces errors coupled into the sensor from the driven mode, and allows for independent optimization of the driving and sensing elements.

The EOM's for this device are calculated similarly to section III, with the difference that there are now more generalized coordinates for the device during the calculation. After the calculation, constraints are placed on the extra coordinates. There are x and y positions for the inner mass with respect to the outer frame, x_i and y_i, and x and y positions for the outer frame with respect to the origin of the local frame, x_o
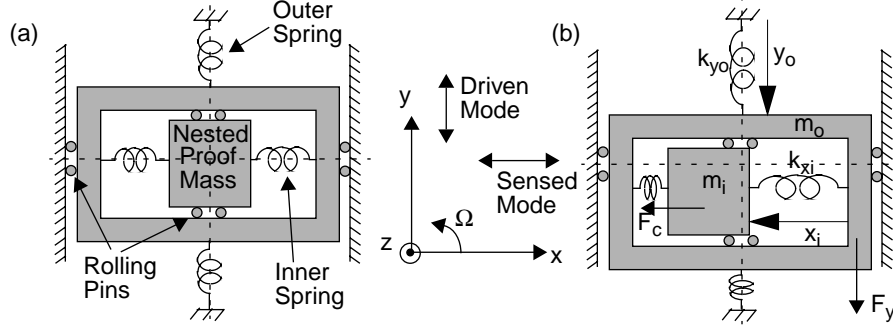
21

Fig.15 - Schematic view of the elastically gimbaled gyroscope, (a) stationary, (b) under forces in *x* and *y*.

and y_o. These local coordinates have corresponding global coordinates, q_i, p_i, q_o, and p_o, related to them as follows (α and ϕ have been omitted for brevity):

$$q_o = x_o \cos\theta - y_o \sin\theta + r_x \tag{26}$$

$$p_o = x_o \sin\theta + y_o \cos\theta + r_y \tag{27}$$

$$q_i = x_i \cos\theta - y_i \sin\theta + r_x \tag{28}$$

$$p_i = x_i \sin\theta + y_i \cos\theta + r_y \tag{29}$$

The potential energy is:

$$PE = \frac{1}{2}(k_{xo}x_o^2 + k_{yo}y_o^2 + k_{xi}x_i^2 + k_{yi}y_i^2) \tag{30}$$

where k_{xo} and k_{yo} are the spring constants in x an y of the outer springs, and k_{xi} and k_{yi} are the spring constants for the inner mass.

The kinetic energy expression is:

$$KE = \frac{1}{2}(m_o \dot{q}_o^2 + m_o \dot{p}_o^2 + m_i(\dot{q}_o + \dot{q}_i)^2 + m_i(\dot{p}_o + \dot{p}_i)^2) \tag{31}$$

Using these equations along with equation (7), the simplified EOM's for this gyroscope, after the rolling pin conditions constraining x_o and y_i to be zero are taken into account are:

$$\ddot{x} = -\omega_x^2 x - \frac{\omega_x}{Q}\dot{x} - \frac{F_x}{m_i + m_o} + x\Omega^2 - m_i\frac{(y\dot{\Omega} + 2\dot{y}\Omega)}{m_i + m_o} + \frac{2m_i + m_o}{m_i + m_o}(a_x \cos\theta - a_y \sin\theta) \tag{32}$$

$$\ddot{y} = -\omega_y^2 y - \frac{\omega_y}{Q}\dot{y} + 2\Omega\dot{x} + y\Omega^2 + x\dot{\Omega} - 2(a_x \sin\theta - a_y \cos\theta) \tag{33}$$

with a drive function of

$$F_x = F_d \sin(\omega_x t) \tag{34}$$

The distinguishing characteristic of this design is that the oscillation of the inner proof mass is com-

22

pletely mechanically decoupled from the oscillation of the outer frame. Moving the inner mass with respect to the outer frame does not affect the motion of the outer frame (to first order). This decoupling has two distinct advantages. The first advantage is that decoupling results in a easily optimizeable system. Since, motion along one axis does not affect motion along the other axis, the internal and external elements can be optimized independently. For example, this device can be modified and run in a configuration whereby an accelerometer can be used as the center element. This accelerometer can be optimized to measure the Coriolis acceleration.

The second advantage is in mechanical crosstalk. In some gyroscope designs, including the 3FSG above, the motion of the excited mode can be mechanically coupled into the sensed mode through comb-drive motion, non-orthogonal oscillations and force, and other means. The excited mode of the device experiences a relatively large displacement, 1.5 μm, so even if only a fracti0n of that motion is coupled into the sensed mode, it could be larger than the 10's of picometer displacements that the Coriolis force produces. This design completely separates the two modes of oscillation, thereby eliminating mechanical crosstalk.

C. Design

Again, the prototypes were designed for structure testing purposes. The design process began by sizing the driven mode to achieve a visible oscillation (if given sufficient voltage). The internal and external elements must be sized simultaneously in order to keep the resonant frequencies matched.

The EGG has an inner spring constant in both the x and y directions, and an external spring constant in both directions. Ideally, the outer frame is suspended by springs that are compliant in x, but infinitely stiff in y, and *vice versa* for the inner mass. The residual stress in the microstructures necessitates the use of stress relief for long beams. Therefore, instead of simple beams being used in the EGG, a crab-leg suspension is used.

An entire crab-leg suspension (4 crab legs) with constant width has spring constants of [13]

$$k_y = \frac{Ehw_a^3(l_b + 4l_a)}{l_a^3(l_b + l_a)} \quad k_x = \frac{Ehw_b^3(4l_b + l_a)}{l_b^3(l_b + l_a)} \tag{35}$$

where w_b and l_b refer to the width and length of the longer beam of the suspension, and w_a and l_a refer to the width and length of the shorter segment of the suspension, the thigh.

Excited-mode specifications are determined using (20) and (21) from the 3FSG design section, section IV-C. The inner crab-leg springs on the EGG are 180μm in length, 2.1μm in width, and 5μm in height, with a 12μm thigh on the crab-leg. For the CMOS-MEMS process, Young's Modulus, E, is 62GPa. The inner suspension then has a spring constant of 1.88 N/m in the x-direction, and 1972.9 N/m in the y-direction. The outer suspension crab-legs are 146μm in length, 2.1μm in width, and have a thigh length of 12μm. The outer spring constants are 3.48 N/m in the y-direction, and 2039 N/m in the x-direction. The actuators have 40 comb fingers, separated by a gap of 1.5μm, and a height of 5μm. When driven by 10 V, the actuators produce a force of 0.134μN. The resulting maximum displacement of the excited mode, with a Q of 50, is then 1.93μm. Using (14) from section III, the displacement current from the excited mode sensor will have an amplitude of 2.28×10^{-9} A which will result in a voltage of 2.28mV at the output of a transimpedance amplifier with a gain of 1×10^6.

Equations (17) and (18) from section IV-B are used here to predict the magnitude of the sensed-mode displacement given the mass, m, the mode's resonant frequency, ω_{ry}, the external rotation rate, Ω, the Q factor of resonance, and the spring constants in both modes. This calculation also assumes that the resonant frequencies are matched well.

For operation of the device in the matched mode, the resonant frequencies of the modes must be nearly equal. The modal frequencies are matched by sizing the springs, the outer frame, and the proof mass simultaneously in order to meet the constraint derived from the EOM's,

$$\omega_y = \sqrt{\frac{k_y}{m_i + m_o}} = \omega_x = \sqrt{\frac{k_x}{m_i}} \tag{36}$$

Because of the complexities of the process, and the need to have relatively large holes in concen-

24

trated plate masses, this matching is more difficult. One useful layout and design item is an "atomic" mass element. This mass element is simply a small square piece of mass with a square hole in it, and has an effective density. Equation (36) can be simplified, assuming uniform thicknesses and Young's Modulus, to:

$$\frac{w_y^3 L_x^3}{L_y^3 w_x^3} = \frac{\rho_i w_i h_i + \rho_o w_o h_o}{\rho_i w_i h_i} \tag{37}$$

If the densities of the inner and outer masses are the same, then density drops out of the equation, and the design process comes down to sizing widths and heights, without worrying about effects of release holes. Use of the "atomic" mass elements assure this consistent density of the outer and inner plate masses.

The inner mass on the EGG is a 250μm by 250μm mass rearranged in such a way as to put mass on the actuators and sensors, and to reduce the overall area taken up by the device. The effective density of the composite microstructure is taken to be approximately 2600kg/m^3. The proof mass has a mass of 0.8125μg, yielding an inner resonant frequency of 48.1krad/s, or 7.7 kHz. The outer frame is 500μm long, 370μm wide, with segments having a width of 20μm. The outer frame's mass is then 0.432μg. The effective mass of the outer mode includes the mass of the outer frame, the inner mass, the inner springs, and comb fingers, and has a calculated resonant frequency of 51.96krad/s, or 8.3kHz. When an external rotational rate of 1°/sec is applied, the resulting Coriolis force, using (17), on the inner mass is 2.77pN. The resulting displacement of the sensed mode, using (18), is 73.7pm. Using (13) from section III, the final sensitivity for the EGG is 18.43μV/°/sec.

Equations (24) and (25) for Brownian noise were given in section IV-C, and will be used here. Using (25) from section IV-C, for a bandwidth of 100 Hz, and at a temperature of 300K, the Brownian noise in this device is estimated to be 0.31°/sec.

VI. Modeling and Simulation

A. Introduction

As MEM systems increase in size and complexity, it becomes increasingly harder to analyze the device by hand. The development of CAD tools for these devices in an important step in the acceptance

25

and proliferation of this technology. The gyroscope is an intermediate system that provides a good testbed for simulation tools. Here, we have focused on hierarchical nodal simulation of the entire multidomain gyroscope system.

NODAS (Nodal Design of Actuators and Sensors) [9][10][12] is a set of nodal models, and a methodology for their use, intended to be used in the Saber nodal simulator [15][16]. These models are set up in such a way that they can be connected together and simulated in a fashion similar to current electronic circuit simulation. NODAS offers three main advantages over other simulation methods: high simulation speed, simulation of multi-domain systems, and implementation of design hierarchy. Jan Vandemeer's master's thesis [12] for the Electrical and Computer Engineering Department at Carnegie Mellon offers a detailed explanation of the NODAS methodology.

Much MEMS simulation is performed through finite element analysis (FEA). FEA breaks the structure into many pieces, hence operating slowly and needing much memory. Nodal simulation uses larger pieces of the structure and therefore reduces the number of nodes, simulation time, and memory requirements. Multidomain FEA simulation also requires the use of coupled simulators (*i.e.* mechanical and electrostatic) and iterates over solutions until there is a convergence. Nodal simulation performs multi-domain simulation simultaneously. Finally, nodal simulation allows the use of simple components that can be modeled to a high accuracy. These simple components, when connected into larger devices, result in a simulation that accounts for many of the more complex effects between nodes, but does not model global interactions between elements. These components can be grouped into subcircuits and placed into even larger system simulations, much like in electronic design automation.

During the development of NODAS, models have been developed for various components vital for the simulation of inertial sensors, specifically gyroscopes. A general method for including effective mass in an arbitrary beam was developed to improve the accuracy of resonant frequency simulation. Finally, global rotational effects on a mass were included to account for the Coriolis force and other psuedoforces that should occur.

B. Important Models in Gyroscope Simulation

i. Beam Effective Mass

A beam, when bending, exhibits an inertial force, but this force is not the same amount as in rigid-body translation. This inertial force on the beam must be taken into account when designing an inertial device. The traditional method of calculating the effective inertial force of a beam is by integrating over the velocity of each part of the beam to get a kinetic energy, and then extracting an effective mass. This method relies on knowing the exact shape of the beam as it undergoes a periodic motion. That shape is not known *a priori* in a nodal simulation where there is only information about the ends of the beam at one instant in time. Therefore, a method for including the effective mass of a beam undergoing an arbitrary bending shape was developed.

A Lagrangian analysis is performed on the beam to determine its equations of motion with respect to the two nodes at the end of the beam. The state variables for the system are taken to be the variables at the ends of the beam. The potential energy of the beam is related to the spring constant, and the kinetic energy is found by integrating over a shape function that is determined by the state variables.

A simple beam in quasi-static motion has an approximate shape

$$y = ax^3 + bx^2 + cx + d \tag{38}$$

In a nodal sense, we know the following coordinates at the ends of the beam

$$y(0) = y_a \quad y(l) = y_b \tag{39}$$

$$\frac{dy}{dx}(0) = \theta_a \quad \frac{dy}{dx}(l) = \theta_b \tag{40}$$

These four equations can be simultaneously solved to find the shape of a beam given an arbitrary set of values at its endpoint coordinates

$$y = \left(\frac{l\theta_a + l\theta_b + 2y_a - 2y_b}{l^3} \right) x^3 + \left(\frac{-2l\theta_a - l\theta_b - 3y_a + 3y_b}{l^2} \right) x^2 + \theta_a x + y_a \tag{41}$$

The velocity of each point of the beam is a simple time derivative. Only the endpoint variables are time dependent in this situation

$$\dot{y} = \left(\frac{l\dot{\theta}_a + l\dot{\theta}_b + 2\dot{y}_a - 2\dot{y}_b}{l^3} \right) x^3 + \left(\frac{-2l\dot{\theta}_a - l\dot{\theta}_b - 3\dot{y}_a + 3\dot{y}_b}{l^2} \right) x^2 + \dot{\theta}_a x + \dot{y}_a \tag{42}$$

The kinetic energy (translational plus rotational) of this beam is then calculated as

$$dKE = \frac{1}{2}\rho tw\dot{y}^2 dx + \frac{1}{24}\rho wt^3 \left(\frac{d}{dt}\left(\frac{dy}{dx}\right) \right)^2 dx \qquad KE = \int_0^l dKE \tag{43}$$

where ρ is the density of the beam, t is the thickness of the beam, and l is the length of the beam.

The Lagrangian is created and equations of motion (EOM's) are derived using Lagrange's equation (7). The generalized coordinates are y_a, y_b, θ_a, θ_b, yielding the following EOM's:

$$F_{y_a} = \rho tw \frac{((132l^3 + 21lt^2)\ddot{\theta}_a + (-78l^3 + 21lt^2)\ddot{\theta}_b + (936l^2 + 252t^2)\ddot{y}_a + (324l^2 - 252t^2)\ddot{y}_b)}{2520l} \tag{44}$$

$$F_{y_b} = \rho tw \frac{((78l^3 - 21lt^2)\ddot{\theta}_a + (-132l^3 - 21lt^2)\ddot{\theta}_b + (324l^2 - 252t^2)\ddot{y}_a + (936l^2 + 252t^2)\ddot{y}_b)}{2520l} \tag{45}$$

$$M_{y_a} = \rho tw \frac{((24l^4 + 28l^2t^2)\ddot{\theta}_a + (-18l^4 - 7l^2t^2)\ddot{\theta}_b + (132l^3 + 21lt^2)\ddot{y}_a + (78l^3 - 21lt^2)\ddot{y}_b)}{2520l} \tag{46}$$

$$M_{y_a} = \rho tw \frac{((-18l^4 - 18l^2t^2)\ddot{\theta}_a + (24l^4 + 28l^2t^2)\ddot{\theta}_b + (-78l^3 + 21lt^2)\ddot{y}_a + (-132l^3 - 21lt^2)\ddot{y}_b)}{2520l} \tag{47}$$

The beam is modeled as a flexure with two masses, one on each end. These masses do not have a constant value, but change as the beam flexes, When implemented in Saber, these inertial force terms are added to the elasticity terms [17][19], resulting in a simple mass spring system.

ii. Global Rotation Effects

In the current NODAS framework, each element has a set of nodes that describes its position relative to the frame of reference of the chip. In that way, measurements can be made of displacements with respect to other nodes on the same chip. There is also a set of nodes that tracks the rigid-body position of each element with respect to the global frame of reference, from which all inertial effects are determined. These two sets of nodes completely describe each element's position and orientation with respect to the global frame of reference.

The value of the global position nodes, $\dot{x}_g$, represent exactly where the rigid-body position of the

elements are with respect to the global frame, but the local displacement nodal values, $\vec{x}_l$ need to be rotated into the global frame and then added to the global positions to calculate the position and displacement of each node in the global frame of reference

$$\vec{X}_g = \vec{x}_g + \underset{\sim}{\Omega}\vec{x}_l \tag{48}$$

where $\underset{\sim}{\Omega}$ is a rigid body rotation matrix relating the local frame to the global frame.

The equation of motion for the mass is $F=ma$, where a is the acceleration in the global frame of reference. This acceleration is calculated by taking a double derivative of the above expression within the simulator. The global forces that are calculated are then rotated back into the local frame of the chip. Therefore, the following equation is implemented in the simulator for a plate-mass model

$$F = \underset{\sim}{\Omega}^{-1}m\left(\frac{d^2\vec{x}_g}{dt^2} + \frac{d^2}{dt^2}(\underset{\sim}{\Omega}\vec{x}_l)\right) \tag{49}$$

C. Three-Fold Symmetric Gyroscope System Simulation

The 3FSG (Figure 16) uses several different lumped-parameter components in its simulation. The fundamental component is the central plate mass. This mass uses the full global-rotational-effects model and hence is where the Coriolis force is developed. This mass is connected to the outer masses by beams. These beams include the effective mass method described earlier. The outer masses in the 3FSG simulation use simpler models that do not include rotational effects. This was done to speed up the simulation by reducing the number of variables and nodes. Comb-drive models complete the mechanical schematic by converting mechanical motion to an electrical signal.

The outputs of the output comb drives are electrically connected to transimpedance amplifiers, modeled using ideal opamps and resistors from the standard component library packaged with the simulator. The control signal from the driven-mode sensor is used as input to a phase-locked loop, and as the signal with which the sensed mode is demodulated. The output signals from the sensed mode are subtracted from each other to remove undesirable common-mode signals, and then multiplied with the output from the

driven mode. Following this multiplication is a filter that removes the higher frequency terms leaving only
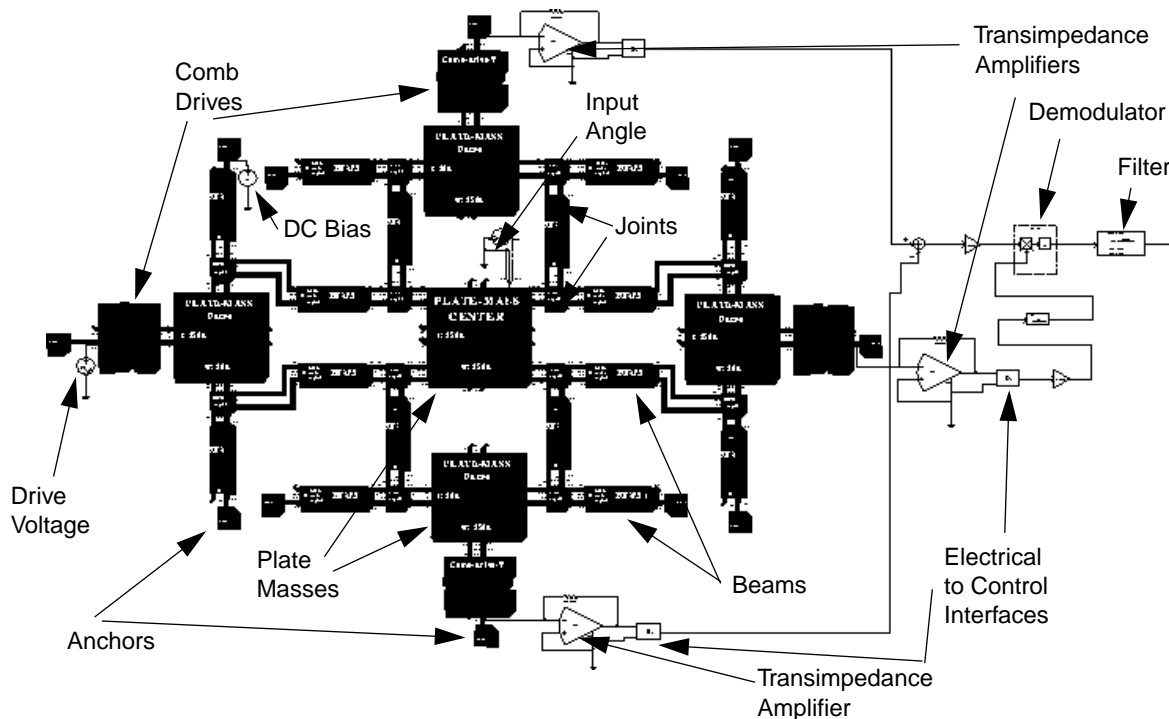
the demodulated output of the sensor.

Fig.16 - Schematic of the three-fold symmetric gyroscope for nodal simulation.

An AC analysis (Figure 17) is performed first to extract the resonant frequency of the structure in the

excited mode, which was found to be 10.3 kHz. The frequency of the sinusoidal voltage source is set at this

resonance frequency. The amplitude of the source is 10V. The angular input source is set at a magnitude of

1 radian, with a frequency of 50 Hz, corresponding to 2866°/sec. This is a rather large signal that is used

for purposes of visibility on the plots. A transient simulation is performed over a time range that covers one

complete cycle of the input angle source, 0.1 seconds, using 2µs timestep (1/50 of the period of the input

sinusoidal voltage).

The simulation took 1100 seconds to complete on a double processor 200MHz UltraSparc2, and

covered 4053 timesteps with an average duration of 5µs. Figure 18d is a plot of the displacement of the

excited mode of the device. Figure 18c shows the displacement of the sensed mode of the device undergo-

ing the above rotation. Figure 18b is the input signal to the device. The excited mode has an amplitude of
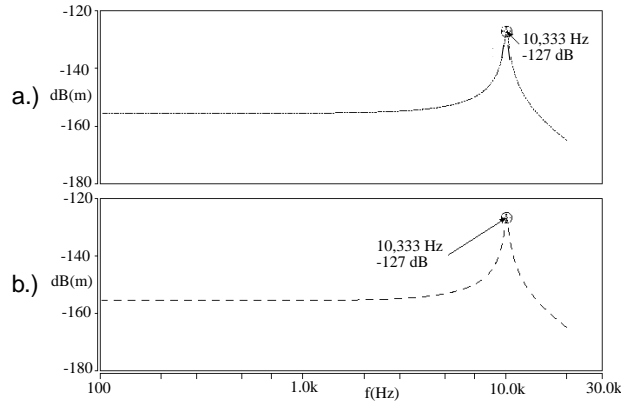
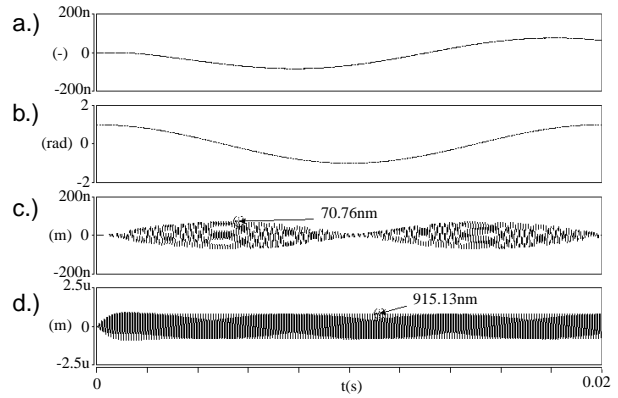Fig. 17 - AC analysis of the 3FSG, a.) Sensed mode, b.) Excited mode.

Fig. 18 - Transient analysis of the 3FSG, d.) Displacement of the excited mode, c.) Displacement of the sensed mode, b.) The Input angle, a.) The output of the device.

915.13nm in this simulation, and the sensed mode has a maximum displacement of 70.76nm. The sensed mode displacement corresponds to 24.6pm for a 1°/sec rotational rate. The demodulated output signal is shown in Figure 18a. In the output signal, the phase delay due to the filter can be seen in that the maximum rotational rate is output about 0.003 seconds after the rotation input crosses zero (the point of maximum rotational rate).

These values for the displacements are lower than what was expected in the design of the structure in section IV-C. The main problem is evident from the AC analysis. The AC analysis shows a resonant frequency of 10.3 kHz, with a 29dB gain over the static displacement. From this analysis, a Q-factor of 29.1 is extracted. In the simulation, only air damping is modeled, and not internal friction due to the composite structure. Also, this simulation does not take place in a vacuum. So, the Q-factor used in the design, 50, is 1.7 times what was found in the simulation, resulting in displacements that are 1.7 times less than expected for a 2866°/sec rotation.

A second point worth noting is seen at the point in the output where the rotational rate goes to zero, where the oscillation of the sensed mode should drop to zero. Another simulation was run with a zero input rotational rate, and a small bias appeared (Figure 19). The central mass shows attometers of motion (Figure 19e), a very small signal that may result from numerical error. The top sensor shows motion in both x (Figure 19d) and y (Figure 19a), both of which are expected. The x motion is from the small compliance in the
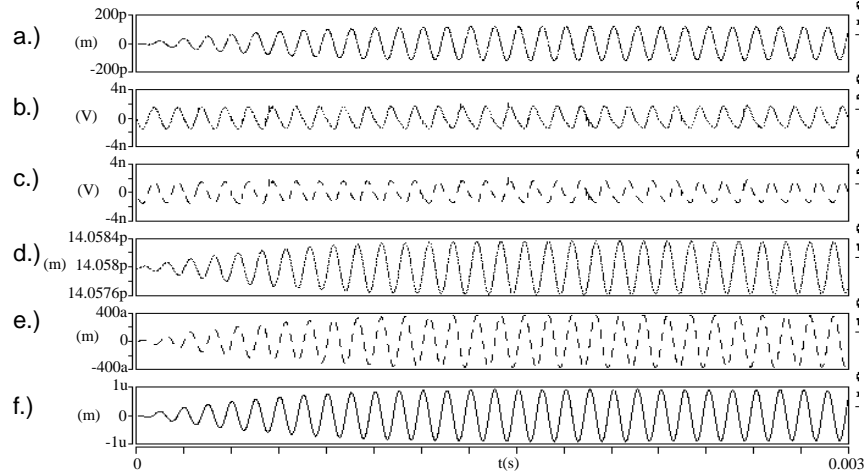
31

Fig. 19 - Transient analysis of the 3FSG with zero input, f.) Displacement of the excited mode, e.) Displacement of the sensed mode, d.) Displacement of the top sensor in *y*, c.) Electrical output of the top sensor, b.)Electrical output of the bottom sensor, a.)Displacement of the top sensor in *x*.

beams that are used to stop the sensors from moving in *x*. The motion in *y* is from the second-order deflections described earlier. These motions create electrical signals in the sensors that could swamp the Coriolis signal. However, from Figures 19c and 19b, it can be seen that these extra signals are common-mode signals between the top and bottom sensor, and can be cancelled.

D. Elastically Gimbaled Gyroscope System Simulation

The simulation of the elastically-gimbaled gyroscope (Figure 20) is very similar to the 3FSG. Again, the central-mass model includes rotational effects, while the components used in the outer frame are beams with mass, but no rotational effects. Reduction in simulation time was again the motivation for simplifying the component models. The sensing elements operate in the same manner as in the 3FSG.

An AC analysis (Figure 21) is performed first to extract the resonant frequency of the structure in the excited mode, which was found to be 8.3 kHz, and for the sensed mode which was found to be 7.7 kHz. The frequency of the sinusoidal voltage source is set at the resonant frequency of the excited mode. The amplitude of the source is 10V. The angular input source is set at a magnitude of 1 radian, with a frequency of 50 Hz, for the same reasons as in the 3FSG. A transient simulation was performed over a time range of 0.11 seconds, using 2μs timesteps (1/50 of the period of the input sinusoidal voltage). The results are shown in Figure 22.
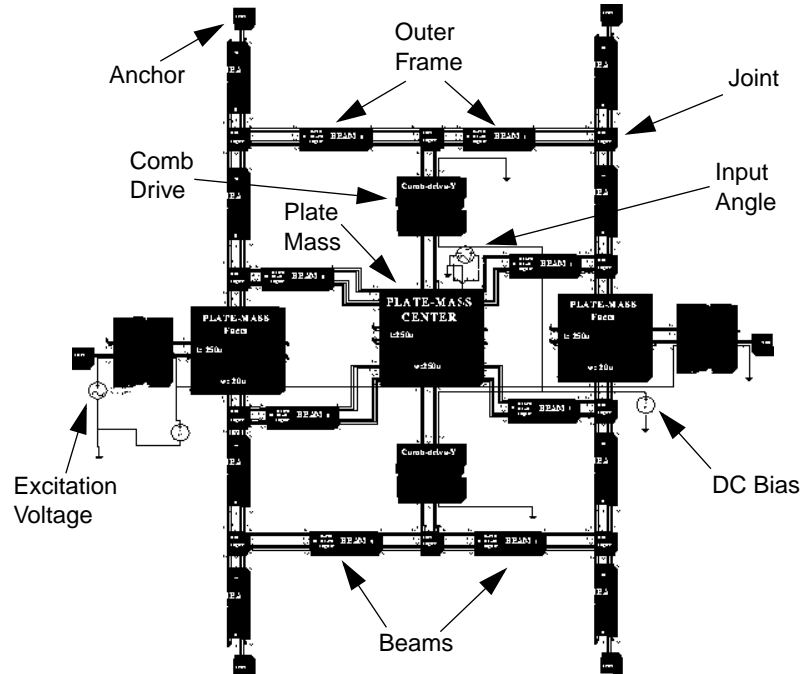
32

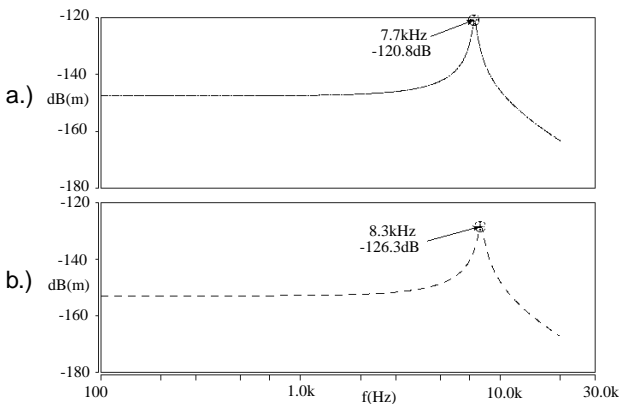Fig. 20- Schematic of the elastically-gimbaled gyroscope for nodal simulation.

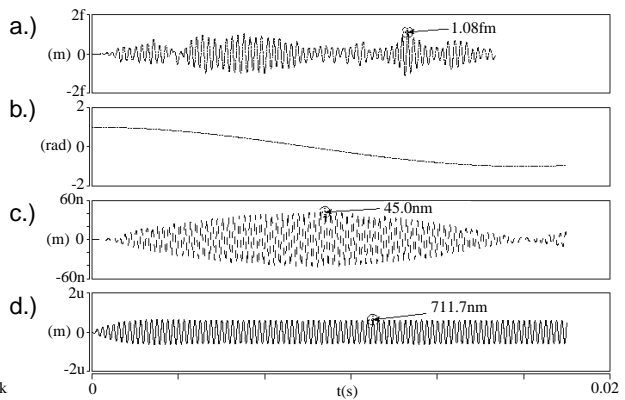Fig. 21- AC analysis of the EGG, a.) Sensed mode, b.) Excited mode.

Fig. 22- Transient analysis of the EGG, d.) Displacement of the excited mode, c.) Displacement of the sensed mode, b.) The input angle, a.) Displacement of the sensed mode with zero input to the device.

The simulation took 888 seconds to complete on a double processor 200MHz UltraSparc2, averaging timesteps of 6.25 µs and taking 0.45 seconds per each timestep. Figure 22d shows the displacement of the excited mode, which had an amplitude of 711.7nm. Figure 22c shows the amplitude of the sensed mode when experiencing the above rotation. It had a maximum amplitude of 45.0 nm. Figure 22b is a plot of the angle input. Again, the values for the mode displacements are smaller than what would be expected for this rotational rate. As in the case of the 3FSG, this can be explained in the Q-factor. For this device, Q-factors

of 18.8 for the excited mode and 24.2 for the sensed mode were extracted from the AC analysis. Both of these values are smaller than those used in the design.

Figure 22a shows the output of the device when there is zero-input rate. This plot shows a signal at the same frequency of the excitation, but its amplitude is on the order of femtometers. The seemingly random envelope of the signal suggests some sort of numerical error.

E. Simulation Issues

The first major issue is that of simulation time. A number of factors affect the time it takes to simulate a complex system like a gyroscope. The first factor is the number of nodes on the system. The more nodes, the more calculations need to be performed per each iteration. This system uses many similar components, so if the number of nodes can be reduced on one component, it is likely that there will be a large effect on the schematic. For example, the joint model is a common component in the simulation. The joint model originally had four ports, but in lots of cases, only three ports are needed. A new three-port model was created, greatly reducing the size of the system. For the 3FSG, there are 12 joints, and the fourth port has 7 nodes. By using three-port joints, the number of nodes is reduced by 84. This reduced simulation times by 0.02 seconds per timestep. With a simulation of 4053 timesteps, this reduces simulation time by 80 seconds. Similar improvements can be made by reducing the number of unused ports on the plate masses.

A second major issue is that of high-frequency transients. Even though the system is being excited by a signal in the 10kHz range, there can be signals in the MHz range during the beginning of the simulation because of extraneous oscillations in the structure (*i.e.*, longitudinal oscillations of beams). The simulator will see these signals and reduce the time step to accommodate for them, drastically increasing simulation time. In the above schematic, initial transients drop the timestep to on the order of nanoseconds, when the main signal of interest is on the order of 5µs. The simulator offers a method, the minimum timestep, for reducing this effect. This tells the simulator to not take time steps below a certain value; in the above schematic, that value was 0.5µs. Therefore, any signals with a period below the minimum time step

are neglected by the simulator.

The schematic itself can be setup to help avoid the excitation of any high-frequency transients. A common issue deals with the angular input source to the device. This is the source that tells the system that it is experiencing an external rotation. The sine angle source is actually zero-valued at all times before the simulation begins. But, at t=0, there is a discontinuity in the derivative of the sine source, it has its maximum derivative at t=0. This discontinuity in the derivative is, mathematically, a sharp discontinuity in the rotational rate, and creates a large initial Coriolis force which excites the sensed mode for a short time. A cosine source was created for this purpose. Using a cosine source greatly reduced the start-up time of the simulation.

Even with the above improvements, the simulation is still long because of the very nature of the device. The device fundamentally operates at a high frequency compared to the signal that is intended to be measured. For example, the gyro may operate at 10kHz, but measure a rotation with a frequency of 10 Hz. If the simulation is run over a full cycle of the input angle, the simulation must go through many timesteps because the timestep must be small enough to account for the high-frequency excitation of the structure.

A similar problem, though not seen in this simulation, is related to a different configuration of the electronics. If the electronics are set up as a capacitive voltage divider with a very high frequency carrier signal (*i.e.*, 1MHz), the simulation must then take timesteps small enough to get the carrier signal, but must run for long enough to reach a full cycle of the input angle. Because of the difference in frequency of the signals, this simulation could take a totally impractical amount of time and computer resources.

VII. RESULTS

The initial 3FSG design has been fabricated and released. A SEM of the device is shown in Figure 24. The curl of the structure has made the device useless, however. The plate mass scrapes along the substrate, creating more friction than the actuators can overcome. The scraping is evident on the SEM by the lighter square region seen in the center of the proof mass.
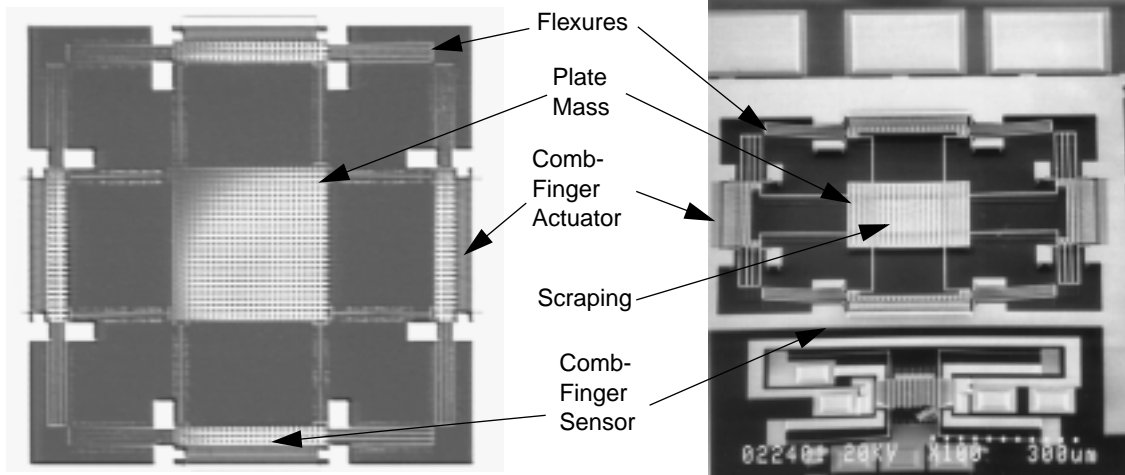
Fig. 23 - Optical Micrograph of the first generation three-fold symmetric gyroscope.

Fig. 24- SEM of the first generation three-fold symmetric gyroscope.

The second generation of the 3FSG has been successfully released (Figure 25) and electrostatically actuated, but the only one available has been fabricated in the 0.8μm CMOS process. Therefore, any results will not match calculations and simulation, but does show the performance of the doubly gimbaled frame. One mode had a resonant frequency of 20.26 kHz. The other mode could not be run because of mis-aligned comb drives. Displacements of the operable mode were approximately 3.8μm when excited by a 20V peak to peak sinusoidal voltage. A approximate *Q*-factor of 21 was measured was calculated. For future work, this device needs to be bonded, run in a vacuum, and tested for sensitivity.

The doubly gimbaled frame on the device did raise the device up from the substrate. However, one pair of comb rotors, the ones situated where the inner frame anchors to the outer frame, are raised completely above the corresponding stator. Figure 26 shows the layout of the device with out-of-plane heights pointed out. Upon measurement, it is seen that the radius of curvature is 9.61mm for the inside frame, and 3.51mm for the outside frame, and the required curl matching did not occur. One possible explanation for this mismatch is that the curvature is related to the width of a structure through the effects of the structure's sidewalls. Future devices should attempt to match widths of components to improve on curl matching.

The first-generation elastically gimbaled gyroscope has been completely released (Figure 27). The resonant frequency has been measured at 9.9kHz for the driven mode, and 9.8 kHz for the sensed mode. A
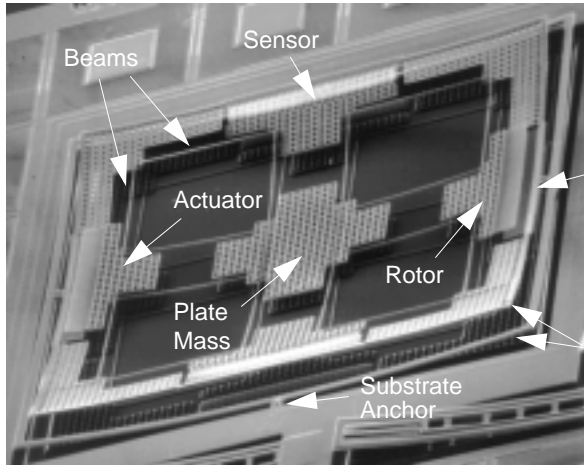
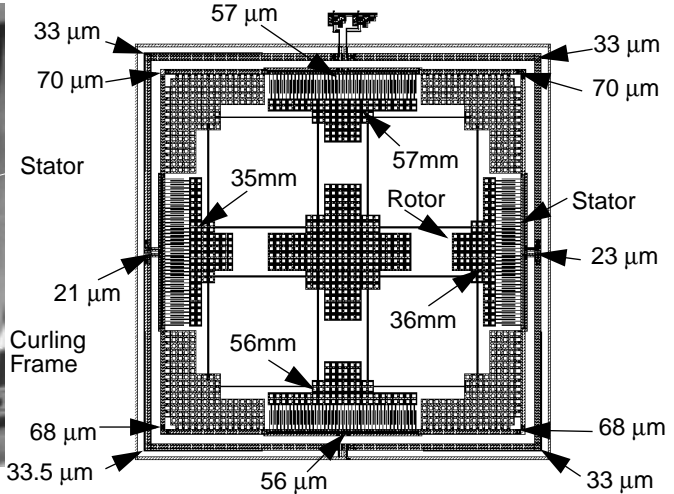Fig. 25 - SEM of the second-generation 3FSG including the doubly-gimbaled frame.

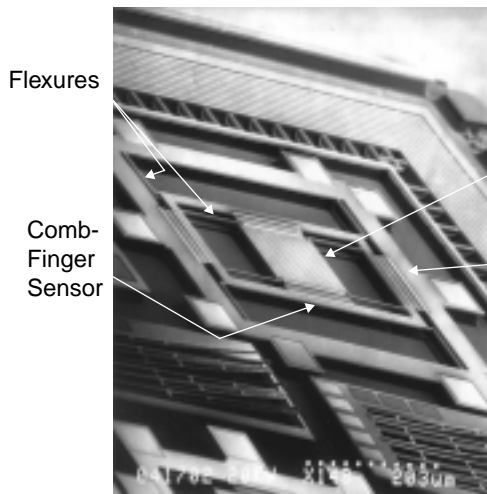Fig. 26 - Out-of-plane heights of various parts of the 3FSG.

Fig. 27- SEM of the first-generation elastically-gimbaled gyroscope.
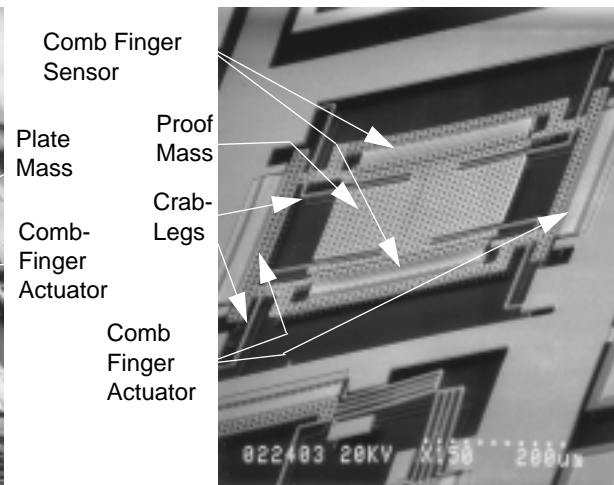

Fig. 28- SEM of the second-generation elastically gimbaled gyroscope without a curling frame.

second generation device (Figure 28), without the curling frame, has been operated and resonant frequencies found at 7.0 kHz for the inner mode and 6.88kHz for the outer mode. The second-generation device's excited mode was operated with an excitation voltage of 12V at resonance and at DC. At resonance, this mode displaced approximately 2.8μm, and at DC it displaced approximately 0.7μm, resulting in a Q of about 4. For verification, the amplitude of the displacement dropped to half at about 105 Hz from the resonant frequency, implying a Q of about 3.25. These measurements were not done in vacuum. Placing the devices in a vacuum will increase the Q-factor. It is also important to note that curling and residual stress had a smaller impact on this device than it did on the 3FSG because of having a released outer frame. The

inner comb-drives match, but the outer ones do not.

VIII. Conclusions

Thin-film vibratory-rate gyroscope mechanisms have been successfully fabricated in an integrated CMOS process. The two designs presented have characteristics which raise sensitivity and cancel undesirable second-order effects. The three-fold symmetric device improves on previous symmetric designs to better match resonant frequencies of the sensed and driven modes to raise sensitivity. Both the three-fold symmetric design, and the elastically gimbaled design are tailored to reduce or eliminate mechanical and electromechanical cross-coupling between the capacitive sensors and electrostatic actuators.

The multiple-conductor microstructures available in the CMOS-MEMS process have the flexibility to allow the implementation of novel mechanisms such as the elastically gimbaled gyroscope. These mechanisms may have advantages over polysilicon-based gyroscopes. However, development of a high-aspect-ratio CMOS-MEMS process is ongoing and must be fully characterized in order to design complex structures, such as gyroscopes, successfully. Curling, for example, is a particular problem which can be characterized, and compensated for in designs. More data needs to be collected on this issue in order to design a curling frame for proper compensation. Also, questions surrounding the Q-factor that can be attained by these devices need to be addressed for proper design and simulation. Regardless, the integration of the 0.5μm CMOS with MEMS provides a powerful paradigm for future high-performance multi-sensor systems.

A simulation methodology has been developed that can accommodate complex multi-domain MEMS systems, specifically gyroscopic systems. Models have been developed that implement important effects in gyroscopes, such as effective mass in beams and global rotational effects. Some simulation issues have been overcome relating to simulation time and accuracy, and many are left to be resolved. For example, the bias seen in the devices with zero input has yet to be explained. However, the tools have already proven beneficial in the design and analysis of inertial sensors, specifically in analyzing structure motion, and in determining resonant frequencies.

Both gyroscopes still need to be tested for operation and sensitivity. They need to be bonded, packaged, put on a breadboard with some signal conditioning electronics, and operated in a vacuum to measure the Q, displacements, and sensitivity. Effects on the signal due to curvature, poor mass distribution, poor elasticity distribution, and other issues need to be explored.

One further item of investigation would be to determine which system configuration would most suit each gyroscope device. For simplicity, both devices were setup for the matched mode, but the separated mode may offer some distinct advantages for some of the devices. The 3FSG fabricated in a polysilicon process will probably be operated in the matched mode. Polysilicon Q-factors can be high (on the order of 10,000), so the sensor would achieve a high gain from Q. Also, the resulting structure is homogeneous, which makes resonant frequency matching more likely. Continued matching of the modes through temperature and time is also more likely in a homogenous material. Therefore, the 3FSG will be better suited to a polysilicon process integrated with electronics.

The EGG must be fabricated in CMOS, where the gains from the Q-factor may not be large enough to offset the advantages in performance offered by operation in the separated mode. The effort required to keep the modes matched in the EGG in the CMOS process through time, temperature, and design may also warrant using the separated mode. The fact that the integration of CMOS electronics with the structure is easily done would benefit the separated-mode configuration. The EGG has fewer springs in its suspension, implying larger displacements, and can also be laid out in a more compact form. These advantages make the EGG well-suited to the CMOS-MEMS process.

One of the main disadvantages of micromachined inertial sensors is the small amounts of mass available. The more mass, the more sensitive the device can be. For surface micromachining using thin films, sensitivity must be increased by increasing the area of the device. However, it is desirable to increase the sensitivity without increasing device size. One idea is to deposit extra material (*e.g.*, a heavy material like tungsten) on top of the central masses of these devices. Large thicknesses of a heavy metal will greatly increase the proof mass, yielding the same increase in sensitivity with no change in the physical dimen-

sions of the device.

IX. Acknowledgments

X. References

[1] J. Bernstein, S. Cho, A.T. King, A. Kourepenis, P. Maciel, and M. Weinberg, "A Micromachined Comb-Drive Tuning Fork Rate Gyroscope," *Proceedings of the Workshop on Microelectromechanical Systems 1993*, pp. 143-148.

[2] Thor Juneau, A.P. Pisano, James H. Smith, "Dual Axis Operation of a Micromachined Rate Gyroscope," *Transducers'97*, Vol.2, pp. 883-886.

[3] William A. Clark, Roger T. Howe, Roberto Horowitz, "Micromachined Z-Axis Vibratory Rate Gyroscope," in the *Technical Digest of the Solid-State Sensor and Actuator Workshop*, Hilton Head, South Carolina, June 2-6, 1996, pp. 283-287.

[4] M. Putty and K. Najafi, "A Micromachined Vibrating Ring Gyroscope," in the *Technical Digest of the Solid-State Sensors and Actuators Workshop*, June13-16, 1994, pp. 213-220.

[5] G.K. Fedder, S. Santhanam, M.L. Reed,S.C. Eagle,D.F. Guillou,M.S. Lu, and L.R. Carley, "Laminated high-aspect-ratio structures in a conventional CMOS process," *Sensors and Actuators*, v.A57, no.2, pp. 103-110.

[6] William C. Tang, Tu-Cuong H. Nguyen, Michael W. Judy, and Roger T. Howe, "Electrostatic Comb Drive of Lateral Polysilicon Resonators," *Sensors and Actuators*, A21-A23, 1990, pp. 328-331.

[7] M. Kranz, G.K. Fedder, "Micromechanical Vibratory Rate Gyroscopes Fabricated in Conventional CMOS," *Symposium Gyro Technology 1997*, Stuttgart, Germany, pp 3.0-3.8.

[8] M.S. Lu, X. Zhu, G.K. Fedder, "Mechanical Property Measurement of 0.5μm CMOS Microstructures," in the *Proceedings of the MRS Spring Meeting Symposium N, Microelectromechanical Structures in Materials Research*, San Francisco, April 15-16, 1998.

[9] J. Vandemeer, M. Kranz, G.K. Fedder, "Nodal Simulation of Suspended MEMS with Multiple Degrees of Freedom," *1997 ASME International Mechanical Engineering Congress and Exposition-Symposium on Microelectrome-*

chanical Systems, vol. 62, pp. 113-118.

[10] J.E. Vandemeer, M.S. Kranz, G.K. Fedder, "Hierarchical Representation and Simulation of Micromachined Inertial Sensors," *Proceedings of Modeling and Simulation of Microsystems*, Santa Clara, CA, April 6-8, 1998.

[11] J.B. Marion, S.T. Thornton, *Classical Dynamics of Particles & Systems*, Harcourt Brace Jovanovich, Inc., 1988.

[12] Jan Vandemeer, *Nodal Design of Actuators and Sensors (NODAS),* M.S. thesis, Department of Electrical and Computer Engineering, Carnegie Mellon University, May 1998.

[13] G.K. Fedder, *Simulation of Microelectromechanical Systems*, Ph.D. thesis, Department of Electrical Engineering and Computer Sciences, University of California at Berkeley, September, 1994.

[14] T.B. Gabrielson, "Mechanical-Thermal Noise in Micromachined Acoustic and Vibration Sensors," *IEEE Trans. on Electron Devices*, ED-40(5):903-909, May 1993.

[15] SaberDesigner Reference, SaberSketch Reference, Release 4.2, Analogy Inc., Beaverton, OR, 1997.

[16] MAST Reference Manual, Release 4.2, Analogy Inc., Beaverton, OR, 1997.

[17] S.P. Timoshenko and J.M. Gere, *Mechanics of Materials, 2nd ed.*, Wadsworth, Belmont, 1984.

[18] MOSIS Submicron CMOS Design Rules.

[19] J.S. Przemieniecki, *Theory of Matrix Structural Analysis*, McGraw-Hill Book Company, 1968.

[20] S.An, Y.S. Oh, B.L. Lee, K.Y. Park, S.J. Kang, S.O. Choi, Y.I. Go, and C.M. Song, "Dual-Axis Microgyroscope with Closed-Loop Detection," in the *Proceedings of the Workshop on Microelectromechanical Systems 1998*, pp. 328-332.

[21] W. Geiger, B. Folkmer, J. Merz, H. Sandmaier, and W. Lang, "A New Silicon Rate Gyroscope," in the *Proceedings of the Workshop on Microelectromechanical Systems 1998*, pp. 615-620.